Molecular-Dynamics Simulations of ELIC—a Prokaryotic Homologue of the Nicotinic Acetylcholine Receptor

Xiaolin Cheng,[†*] Ivaylo Ivanov,[‡§¶‖] Hailong Wang,[**] Steven M. Sine,[**] and J. Andrew McCammon[‡§¶‖]
[†]Center for Molecular Biophysics, Oak Ridge National Laboratory, Oak Ridge, Tennessee; [‡]Howard Hughes Medical Institute, [§]National Science Foundation Center for Theoretical Biophysics, [¶]Department of Chemistry and Biochemistry, [‖]Department of Pharmacology, University of California, San Diego, La Jolla, California; and [**]Receptor Biology Laboratory, Department of Physiology and Biomedical Engineering, Mayo Clinic College of Medicine, Rochester, Minnesota

ABSTRACT The ligand-gated ion channel from *Erwinia chrysanthemi* (ELIC) is a prokaryotic homolog of the eukaryotic nicotinic acetylcholine receptor (nAChR) that responds to the binding of neurotransmitter acetylcholine and mediates fast signal transmission. ELIC is similar to the nAChR in its primary sequence and overall subunit organization, but despite their structural similarity, it is not clear whether these two ligand-gated ion channels operate in a similar manner. Further, it is not known to what extent mechanistic insights gleaned from the ELIC structure translate to eukaryotic counterparts such as the nAChR. Here we use molecular-dynamics simulations to probe the conformational dynamics and hydration of the transmembrane pore of ELIC. The results are compared with those from our previous simulation of the human $\alpha7$ nAChR. Overall, ELIC displays increased stability compared to the nAChR, whereas the two proteins exhibit remarkable similarity in their global motion and flexibility patterns. The majority of the increased stability of ELIC does not stem from the deficiency of the models used in the simulations, and but rather seems to have a structural basis. Slightly altered dynamical correlation features are also observed among several loops within the membrane region. In sharp contrast to the nAChR, ELIC is completely dehydrated from the pore center to the extracellular end throughout the simulation. Finally, the simulation of an ELIC mutant substantiates the important role of F246 on the stability, hydration and possibly function of the ELIC channel.

INTRODUCTION

The nicotinic acetylcholine receptor (nAChR) is a prototypical member of the Cys-loop family of ligand-gated ion channels (LGICs). It aggregates at synapses, where it responds to nerve-released acetylcholine to mediate excitatory transmission throughout the central and peripheral nervous systems (1–3). The nAChR plays important roles in memory, cognition, and sensory perception (4–6), and has emerged as a target for treatment of pain, cognitive impairment, neurodegenerative disease, schizophrenia, epilepsy, anxiety, and depression (7,8).

Over the past several decades, our understanding of the molecular mechanism of nAChR has progressed tremendously. Early work using molecular biological, biochemical, and electrophysiological approaches has shed light on the overall topology (9), ligand-binding mechanism (10), ion conductance/selectivity (11), and channel gating kinetics of the receptor (12,13), but the development of an atomic-resolution structural model has lagged behind. For almost two decades, cryo-electron microscopy (cryo-EM) structures have been the only structural information available. In 2005, a closed-state structural model of the nAChR from *Torpedo marmorata* was obtained and refined to yield a near-atomic 4.0 Å resolution image (14). This structure constitutes an important molecular framework for integrating a large body of previous experimental data. Based on a comparison of the α and nonα subunits in this model, Unwin (14) and Miyazawa et al. (15) proposed the first atomic-level gating mechanism, which they termed ‘‘rotation to collapse of hydrophobic girdle’’.

In the early 2000s, a series of crystal structures of the acetylcholine binding protein (AChBP), a homolog of the ligand-binding domain of the nAChR, emerged from the laboratories of Sixma and Taylor (16–19). These AChBP structures offer important insights into the nature of ligand binding and recognition in nAChRs, and are therefore highly relevant for the development of drugs targeting nAChRs. Without a transmembrane domain, however, AChBP provides only limited information about channel gating and/or desensitization. Recently, a 1.9 Å x-ray structure of the nAChR α subunit extracellular domain in complex with a neurotoxin was determined (20). This crystal structure reveals atomic details of several key elements in the nAChR, such as the main immunogenic region, the signature Cys loop, and a previously unresolved oligosaccharide chain. More strikingly, the structure delineates a highly conserved hydration site buried within the hydrophobic core of the protein, and demonstrates that this unusual feature is important for channel gating.

More recently, an x-ray crystal structure of ELIC, a prokaryotic pentameric LGIC from *Erwinia chrysanthemi*, has become available (21). The ELIC structure shows considerable similarity to that of the nAChR, with a backbone root mean-square deviation (RMSD) of only 2.3 Å for the common core residues. However, a few key differences between the bacterial and eukaryotic LGICs are worth

---

Submitted October 6, 2008, and accepted for publication March 11, 2009.

*Correspondence: xcheng@mccammon.ucsd.edu

Editor: Peter Tieleman.

0006-3495/09/06/4502/12 $2.00

doi: 10.1016/j.bpj.2009.03.018

noting. Sequence comparison shows that ELIC has weak or no conservation in regions where the neurotransmitter binds (see Fig. S1 in the Supporting Material). Moreover, the nAChR contains an N-terminal α helix and a long cytoplasmic domain connecting the M3 and M4 helices, but these two motifs are not present in ELIC. Unlike the nAChR, the transmembrane pore of ELIC is more constricted, with entry of water completely occluded by bulky hydrophobic residues at the pore center. Several loops in the membrane interface region of ELIC, likely involved in transmission of the gating motion, differ substantially from the corresponding region in the nAChR. In ELIC, the $\beta6$–$\beta7$ loop, which lacks the two canonical cysteine residues, cannot be superimposed with the Cys loop in the *Torpedo* nAChR, or that in the $\alpha1$ nAChR, where it adopts a type VIb turn (20). The $\alpha2$–$\alpha3$ linker appears to form a more extended loop. In ELIC, the $\beta6$–$\beta7$ loop and the $\alpha2$–$\alpha3$ linker are 7 Å farther apart compared to the nAChR, as measured by the distances between two highly conserved proline residues (Pro^{120}–Pro^{256}: 15.7 Å vs. Pro^{136}–Pro^{272}: 8.6 Å). Despite these differences, the smaller ELIC structure is sufficient to support proton-dependent channel gating (21,22). This high-resolution structure with both the ligand-binding and transmembrane domains thus provides a useful structural model for investigating the conformational dynamics and gating mechanisms of the Cys-loop family of receptors. However, due to the low sequence homology between ELIC and the nAChR, it remains unclear whether the two receptors operate in a similar way, and how much mechanistic information obtained from this bacterial model can be used to understand its eukaryotic counterparts.

To gain insight into the dynamical behavior of ELIC and how it might differ from that of the nAChR, we carried out molecular-dynamics (MD) simulations. We also performed a simulation of an F246E mutant of ELIC. Sequence alignment indicates that the F→E mutation at the 246 position represents one of the most prominent differences between ELIC and the nAChR in their pore-lining helices (Fig. S1). Therefore, the F246E mutant is simulated to investigate the role of F/E246 in influencing the channel conformation and dynamics. MD simulation provides a useful way to probe the dynamics of proteins, and has been applied extensively in the study of the nAChR and AChBP (23–28). However, only a few studies have described the conformational dynamics of the receptor containing both the ligand-binding and transmembrane domains. A simulation carried out by Law et al. (29) showed a twist-to-close motion in which movements of the C-loop correlated with a 10° rotation and inward movement of two nonadjacent subunits. A subsequent simulation initiated from a homology model of the *Torpedo* nAChR revealed that a large-scale bending motion hinged at the membrane interface might be relevant to channel gating, with a cluster of coupled residues identified as likely mediating the transduction process (30). Wang et al. (31) performed MD simulations to explore the transport of single cations through the channel of the muscle nAChR in the presence of a transmembrane potential. Here we present a comparative analysis of conformational dynamics in ELIC and the human $\alpha7$ nAChR. Our results show that although a global twisting motion is preserved in ELIC, the channel shows increased stability compared to the nAChR. Moreover, various loops in the membrane interface region show different dynamical behaviors and slightly modified dynamical coupling features, suggesting that although they are similar in overall architecture, the two receptors may differ in the precise details of transduction of the allosteric signal.

MATERIALS AND METHODS

Normal-mode analysis

Normal-mode analysis (NMA) was performed with a block-based NMA program as described previously (32) using the AMBER ff99SB force field (33). A distance-dependent dielectric (1/4r) was used with no cutoff for nonbonded interactions. The initial structure was taken from the Protein Data Bank (PDB code: 2vl0). The hydrogen atoms were added by the tLeap module in AMBER8 (34). The system was then subjected to three rounds of minimization. The system first underwent 500 steps of steepest-descent minimization with restraints on all backbone atoms. This was followed by 5000 steps of conjugate-gradient minimization with gradually decreasing restraints on Cα atoms. Finally, the structure was minimized for another 3000 steps with no restraints applied until the RMS gradient reached ~0.01 kcal · mol^{-1} · $Å^{-1}$. The heavy-atom RMSD of the final minimized structure was 1.1 Å from the initial crystal structure.

MD simulations

Before the MD simulations were conducted, the protonation states of protein side chains were adjusted to match the results of *pKa* calculation using the Karlsberg webserver (35). The results indicated that all of the ionizable residues were in their standard states at the physiological pH (~7.0). In the F246E mutant, all of the five Glu residues that are introduced to replace the Phe residues in the wild-type ELIC were predicted to be in the unprotonated state. Although the five charged residues would appear to cause somewhat stronger electrostatic interactions at the extracellular vestibule of the transmembrane pore, the prediction is consistent with the fact that the five Glu residues are exposed to the solvent and are not engaged in hydrogen bonding with other residues. MD simulations were then performed with two ELIC structures (the wild-type and the F246E mutant) embedded in a fully hydrated, 120 Å × 120 Å palmitoyl-2-oleoyl-sn-glycerol-phosphatidylcholine (POPC) bilayer. This resulted in a total of ~300 POPC molecules and ~37200 water molecules. Charge neutralization was accomplished with the addition of 49 Na^+ and 24 Cl^- ions for ELIC, and 51 Na^+ and 21 Cl^- ions for the F246E mutant, resulting in a 0.1 M solution for both systems. The solvated systems then underwent four equilibration steps: 1), 2000 steps of energy minimization with protein backbone fixed; 2), five cycles of a 500-step minimization with decreasing positional restraints on the protein Cα atoms; 3), gradual temperature increase from 50 K to 310 K in 10,000 steps of constant-volume MD (NVT ensemble) simulation with harmonic restraints (with force constant of 3 kcal · mol^{-1} · $Å^{-2}$) on the protein Cα atoms; and 4), 2 ns constant surface-area ensemble MD equilibration with decreasing positional restraints on the Cα atoms. After equilibration, two production runs (27 ns and 20 ns long, respectively) were collected for ELIC, and one 10 ns run was collected for the F246E mutant. The second simulation of ELIC (~20 ns) adopted a slightly modified equilibration protocol (initial temperature increase started from 25 K instead of 50 K, and also by using a different random seed for initial velocity assignment) to propagate a trajectory different from that used in the first 27 ns simulation. MD simulations were performed with the NAMD2 program (36) and the CHARMM27 force field (37). A short-range cutoff of 9 Å was used for nonbonded interactions, and long-range electrostatic interactions were treated with a particle mesh Ewald method (38). Langevin dynamics and a Langevin piston algorithm were used to maintain the temperature at 300 K and a pressure of 1 atm. The r-RESPA multiple-time-step method was employed (39), with time steps of 2 fs for bonded, 2 fs for short-range nonbonded, and 4 fs for long-range electrostatic forces. The bonds between hydrogen and heavy atoms were constrained with the SHAKE algorithm (40). All simulations were conducted on the computer facility at the NCSA Supercomputer Center.

Data analysis

The correlated nature of the atomic fluctuations can be characterized by the cross-correlation coefficient C_{ij}, between atoms i and j:

$$C_{ij} = \langle \Delta r_i \cdot \Delta r_j \rangle / \left(\langle \Delta r_i \cdot \Delta r_i \rangle \langle \Delta r_j \cdot \Delta r_j \rangle \right)^{1/2}, \qquad (1)$$

where Δr_i and Δr_j are the displacement vectors for atoms i and j, respectively. The angle brackets denote an average over the trajectory. The correlation matrix for all Cα atoms in ELIC and the ELIC mutant was calculated using the GROMACS program (41) and displayed as a 2D contour plot with the Origin program (42).

A pseudo S^2 order parameter (43) that describes the relative mobility of two local residues is given by

$$S^2 = \frac{1}{2} \langle 3\cos^2\theta - 1 \rangle, \qquad (2)$$

where $\cos\theta$ is defined as a dot product between the two vectors oriented along the N-H bonds of Val^{35} and Phe^{110}, respectively.

Pore radius profiles were calculated with the HOLE (44) program. Both lateral and radial tilting angles were calculated for all the five pore-lining $\alpha 2$ helices as described previously (30). The density profiles were calculated by binning the z-coordinate positions of the atoms for each species (lipid tail carbon, lipid headgroup nitrogen, phosphorus, ester oxygen atoms, and water oxygen atoms) to construct a histogram. The bin size was 0.2 Å, and density was normalized by the volume of a 0.2 Å wide slab of the simulation box oriented perpendicular to the bilayer normal. The program VMD was used in the visualization and analysis of the results (45).

RESULTS AND DISCUSSIONS

Overall motions

Two independent simulations of ELIC were performed to achieve a statistically more reliable set of simulation data. However, due to the remarkable similarity between the RMSDs of the two trajectories (Fig. S2) and the overall comparable RMSF fluctuation patterns (Fig. S3, a and b), only the results from the 27 ns simulation are discussed here. Fig. 1 *a* illustrates the RMSFs of the Cα atoms from simulations of ELIC (*black line*) and the F246E mutant (*red line*), along with the results from the previous simulation of the $\alpha 7$ nAChR (*green line*) (30). The computed B-factor values are color-coded onto the 3D structure of ELIC (Fig. 1 *b*) and the nAChR (Fig. 1 *c*). Similar fluctuation patterns are evident for the two receptors, although the ELIC structure exhibits overall lower flexibility than the nAChR (Fig. S2). The dynamics of the $\alpha 7$ nAChR, especially in its transmembrane domain, could have been artifactually enhanced by the deficiency of the model (30) as well as by the method used to simulate the structure (46), but we note that most of the increased stability observed in ELIC is not due to these artifacts, but instead has a structural basis, as discussed in more detail below. The region that fluctuates most significantly is the C-loop, consistent with previous experimental and computational studies of the nAChR (23,30) and AChBP (47). Other regions in the ligand-binding domain that display significant flexibility are two connecting loops $\beta 2$–$\beta 3$ and $\alpha' 1$–$\beta 4$ located at the distal end of the protein. Compared with the nAChR, the regions corresponding to the Cys- ($\beta 6$–$\beta 7$) and $\beta 8$–$\beta 9$ loops in ELIC show depressed mobility. The reduced mobility in ELIC can generally be attributed to its more engaged local environment, whereas the corresponding region in nAChR appears more loosely packed, which could indicate a deficiency of the simulated nAChR model (30). We further note that the fluctuations of these two loops in nAChR are not drastically affected by the presence of cholesterol in the simulations (see the two green boxes highlighted in Fig. S3, c and d), probably because of their distance from the cholesterol-binding sites (46).

In our previous simulation of nAChR, considerable motion was seen for two transmembrane regions: the M2–M3 linker and the C-terminus of M3. In our simulation of ELIC, the $\alpha 3$ end still displays significant mobility, despite the fact that the intracellular loop connecting $\alpha 3$ and $\alpha 4$ is completely resolved and also considerably shorter. However, in contrast to the nAChR simulation, only small movements are noted in the $\alpha 2$–$\alpha 3$ linker. Given the fact that the $\alpha 2$–$\alpha 3$ linker adopts a more extended conformation (an eight-residue loop in ELIC versus a five-residue loop in the nAChR), the decreased mobility seems surprising at first sight. However, careful inspection reveals that the increased stability in these regions is due to more extensive van der Waals contacts in these loops in ELIC, where the contact surface area for the $\alpha 2$–$\alpha 3$ linker is ~380 Å^2, which is increased by ~20% compared to the nAChR. The $\alpha 2$–$\alpha 3$ linker in ELIC also makes favorable van der Waals contacts with the $\beta 8$–$\beta 9$ loop from the adjacent subunit. Throughout the simulation, we observe a strong hydrogen bond between Arg^{254} (in the $\alpha 2$–$\alpha 3$ linker) and Glu^{159} (in the $\beta 8$–$\beta 9$ loop), which helps stabilize both the loops and increase the local stability. Of interest, a recent computational study by Brannigan et al. (46) showed that the nAChR may contain a cholesterol-binding site next to the M2–M3 linker, and that occupation of cholesterol would stabilize the nAChR structure. Thus, the dynamics of the M2–M3 linker of the nAChR may be artifactually enhanced by the absence of cholesterol molecules in the simulation (30). Because both the conserved Cys loop and the M2–M3 linker are essential for channel gating in the nAChR, the altered structure and dynamics in ELIC imply that these loops may play different roles in coupling the ligand-binding and transmembrane

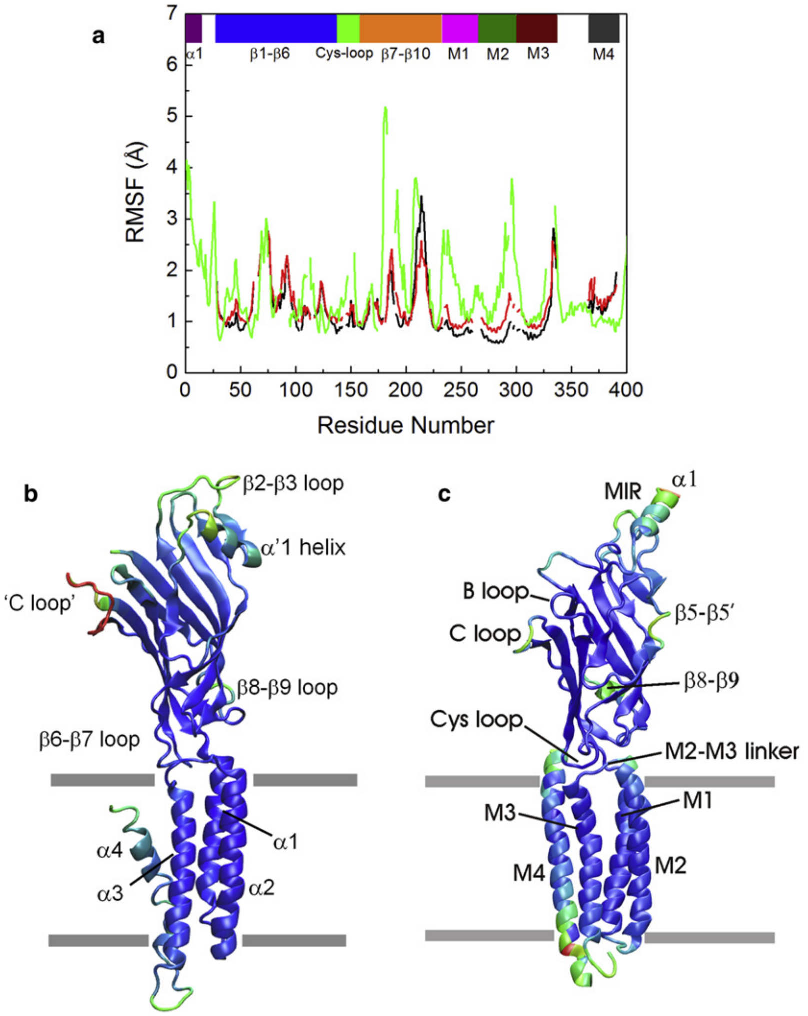

FIGURE 1 (*a*) RMSFs of the Cα atoms from the MD simulation of ELIC (*black line*) along with those from the simulation of the F246E mutant (*red line*) and from the previous simulation (30) of a human α7 nAChR (*green line*). The color bar at the top indicates the sequence position of important structural elements in nAChR; these structural elements are also labeled in *b* and *c*. (*b* and *c*) The computed B-factor values are color-coded on a single subunit of the receptor, with red corresponding to the most mobile region and blue corresponding to the most stable region (*b*: ELIC; *c*: the α7 nAChR from Cheng et al. (30)).

domains. The M4 helix is more peripheral, and major contradictions remain regarding the nature of its dynamics (27,48,49). In our simulation of ELIC, only modest movements are noted in the entire α4 helix, which differs somewhat from previous MD simulations of the α7 nAChR (30,32).

Motion in the extracellular domain is dominated by an asymmetric expansion of the five subunits. At the subunit level, a twisting motion of the extracellular domain, hinged at a hydrophobic region (residue pair Val^{35} and Phe^{110} as shown in Fig. 2 *a*), is evident, in contrast to a bending motion hinged at the junction of β10 and M1 observed in the nAChR simulation (30). Of interest, this hydrophobic site is in a position equivalent to that of a hydration pocket (Thr^{52} and Ser^{126} in Fig. 2 *b*) identified in the recently determined crystal structure of the nAChR α1 subunit in complex with α-bungarotoxin (20). This unusual feature of a hydration pocket buried inside the β sandwich core has been shown to be important for channel function, since mutation of Thr^{52} and/or Ser^{126} to hydrophobic residues substantially reduces gating of the channel (20). Although both Thr^{52} and Ser^{126} are highly conserved among the nAChR family receptors, in ELIC they are replaced by a pair of bulky hydrophobic residues (Val^{35} and Phe^{110}, respectively), in similarity to the AChBPs.

To investigate how this local hydrophobic substitution might affect the overall stability of the receptor, we examined the local structural flexibility at the mutational site in both ELIC and the nAChR. Fast local motions can be sampled with good convergence on the nanosecond timescale of MD simulation. Further, a striking correspondence between motions at different timescales has been revealed by nuclear magnetic resonance studies of adenylate kinase (50). In particular, it has been shown that the fast timescale local hinge motions can dictate the catalytically important global motions. The hydrophobic pair in ELIC is found to stay in contact during the entire length of the simulation. The local conformational flexibility as indicated by the computed order parameters ($S^2 = 0.91$ in ELIC as compared to 0.70 in nAChR α1), clearly shows that the hydrophobic residue pair in ELIC is more rigid than the corresponding pair in the nAChR (Fig. 2 *c*). In the previous simulation of the nAChR, we also found that water molecules inside the cavity are dynamic, with multiple water molecules moving

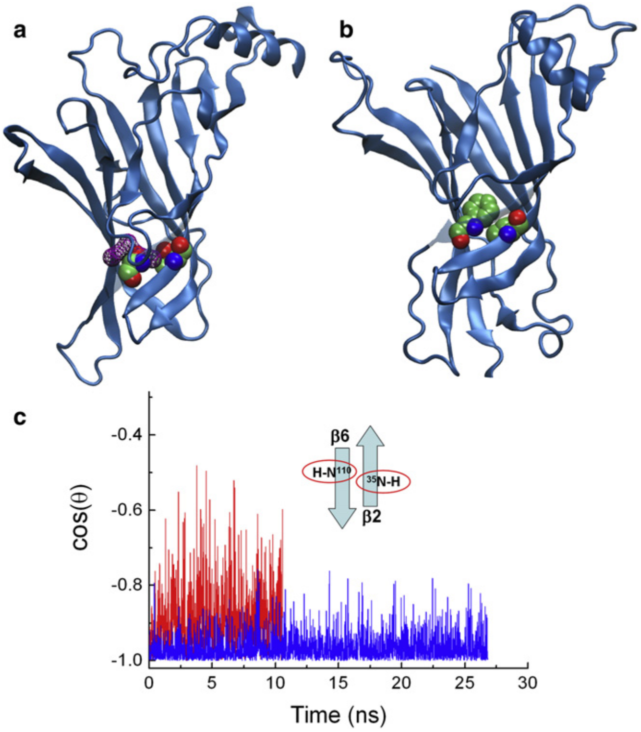

FIGURE 2 (*a*) View from the inside of the nAChR α extracellular domain, showing a hydration cavity with a water molecule hydrogen-bonded to two buried hydrophilic residues (Thr^{52} and Ser^{126}). (*b*) View from the inside of ELIC, showing two bulky hydrophobic residues (Val^{35} and Phe^{110}, respectively) at equivalent positions. (*c*) Time evolution of a local order parameter cos(θ) as a function of time during the simulations of ELIC (*blue line*) and nAChR (*red line*; data obtained from the previous simulation (30)), where θ is defined as a dot product between two vectors along the NH bond in two neighboring residues (Val^{35} and Phe^{110} in ELIC, and Thr^{52} and Ser^{126} in nAChR).

in and out of the cavity. In the hydrophobic cavity of ELIC, no water molecule is found in the crystal structure or during the simulation, and the volume of the cavity fluctuates less. The identified residue pair is near both the Cys- and C-loops, and thus is located in a pivotal position linking the ligand-binding site and the membrane interface region. The locally initiated motion can easily spread to other regions of the protein. The local increased packing in ELIC can therefore contribute to its increased overall stability. These results raise questions as to whether the hydration site is essential for channel gating, and how the bacterial receptors manage to maintain channel gating by switching to a pair of hydrophobic residues. To clarify this issue, it would be interesting to build a chimeric receptor with a ligand-binding domain from ELIC and a transmembrane domain from the nAChR.

NMA

The MD simulations presented here are evidently too short to sample the full gating motion. Therefore, to further characterize the global motion of ELIC, a coarse-grained NMA is employed (32,51). A twist-to-open motion was observed in a number of previous computational studies of the nAChR (32,51,52), suggesting that the motion is robust and probably encoded in the overall topology of the pentameric LGICs. Our NMA analysis of ELIC shows a very similar global twisting motion (Fig. 3 *a*; see Fig. S4 for an animated image) despite the low sequence identity between the two receptors. The correlation coefficient for this mode, relative to the nAChR one, is ~0.8, indicating that the twisting motion shares significant similarity in the two receptors. As described previously (32, 51), this twisting motion involves a concerted, opposite-direction rotation of the ligand-binding and transmembrane domains around the pore axis, with the hinge located at the membrane interface region. In contrast to the nAChR,

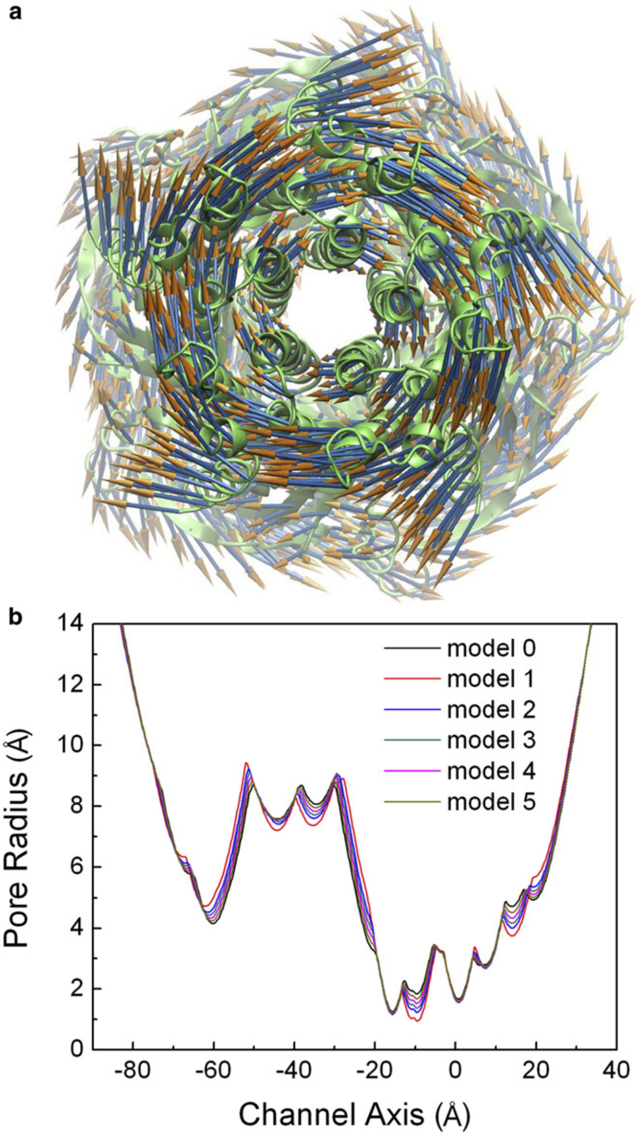

FIGURE 3 (*a*) Global twisting motion of ELIC as suggested by the NMA. The vectors indicating the directions of the motion are shown as arrows mapped on the protein cartoon structure. (*b*) Pore radius profiles of a set of model structures (models 1–5) generated by displacing the closed structure (model 0) along the lowest-frequency mode by various magnitudes.

however, in ELIC the motion does not lead to an ‘‘open’’ channel with a wider pore (Fig. 3 *b*). Detailed inspection reveals that the hydrophobic hindrance at the 246 (20′) position (corresponding to the ~16 Å channel axis position in Fig. 3 *b*) does not decrease at all, whereas the constriction at the 239 (13′) position (corresponding to the ~9 Å channel axis position in Fig. 3 *b*) only opens slightly (< 0.5 Å) via the concerted rotation of the five $\alpha 2$ helices. Therefore, although a very similar global motion is preserved in ELIC, the functional implication of this mode of motion needs to be further assessed.

Dynamical coupling at the membrane interface regions

Dynamical coupling between residues can be analyzed through a covariance analysis of coordinate displacements averaged over the simulation trajectory. Our correlation analysis focuses on the membrane interface regions, including loops $\beta 1$–$\beta 2$, $\beta 6$–$\beta 7$ (corresponding to the Cys loop in the nAChR), $\beta 8$–$\beta 9$, $\beta 10$–$\alpha 1$, and $\alpha 2$–$\alpha 3$ (corresponding to the M2–M3 linker in the nAChR), all of which are known to contribute to channel gating. Overall, the residues appear to be engaged in similar (but not identical) coupling patterns as in the nAChR. Correlation between residues from the $\beta 6$–$\beta 7$ and the $\alpha 2$–$\alpha 3$ loops is most prominent, as shown in an expanded view in Fig. 4 *a*. The same correlation pattern is consistently seen in four out of five subunits. The results reveal a cluster of hydrophobic residues involving Leu^{118}-Phe^{119}-Pro^{120}-Phe^{121} (corresponding to Val^{132}-Phe^{135} in the nAChR) and Leu^{255}-Pro^{256}-Tyr^{257} (corresponding to Pro^{269}-Ile^{271} in the nAChR; Fig. 4 *c*). The Cys loop is highly conserved in the nAChR family receptors, but differs substantially from the corresponding regions in ELIC and AChBP. In the recently determined crystal structure of the nAChR $\alpha 1$ subunit, the Cys loop forms a type VIb turn with one of its central residues, Pro^{136}, adopting an unusual *cis* conformation, whereas in ELIC the $\beta 6$–$\beta 7$ loop shows no secondary structure with the corresponding Pro in a *trans* conformation. ELIC lacks the signature Cys-Cys disulfide bond that joins the $\beta 6$–$\beta 7$ loop in the nAChR and other Cys-loop family receptors. However, the stretch of residues Phe^{119}-Pro^{120}-Phe^{121}-Asp^{122}, located in the center of the loop, is conserved in ELIC. This four-residue motif appears to make extensive van der Waals contacts with the $\alpha 2$–$\alpha 3$ loop and thus shows a strong correlation spot in the map (Fig. 4 *a*). The highly concerted motion of this region suggests that the interactions between the $\beta 6$–$\beta 7$ and $\alpha 2$–$\alpha 3$ loops may contribute to the transduction of binding to gating.

Dynamically correlated residues from the $\beta 6$–$\beta 7$ and $\beta 10$–$\alpha 1$ regions are shown in Fig. 4 *b*. A strong correlation is seen in the lower-right corner of the plot, corresponding to a stretch of residues (residues 121–128) from the $\beta 6$–$\beta 7$ loop/$\beta 7$ strand and residues 190–198 in the $\beta 10$–$\alpha 1$ region, indicating a concerted motion of these two strands. This correlation pattern is very similar to that observed in the previous simulation of the nAChR, which likely reflects the local fold of the protein that couples the motion of the $\beta 7$ and $\beta 10$ strands. A second region reveals correlated motion between Met^{114} from the $\beta 6$–$\beta 7$ loop and Arg^{198} from the $\beta 10$–$\alpha 1$ region. Compared with that in the nAChR, however, the correlation is much more attenuated in ELIC.

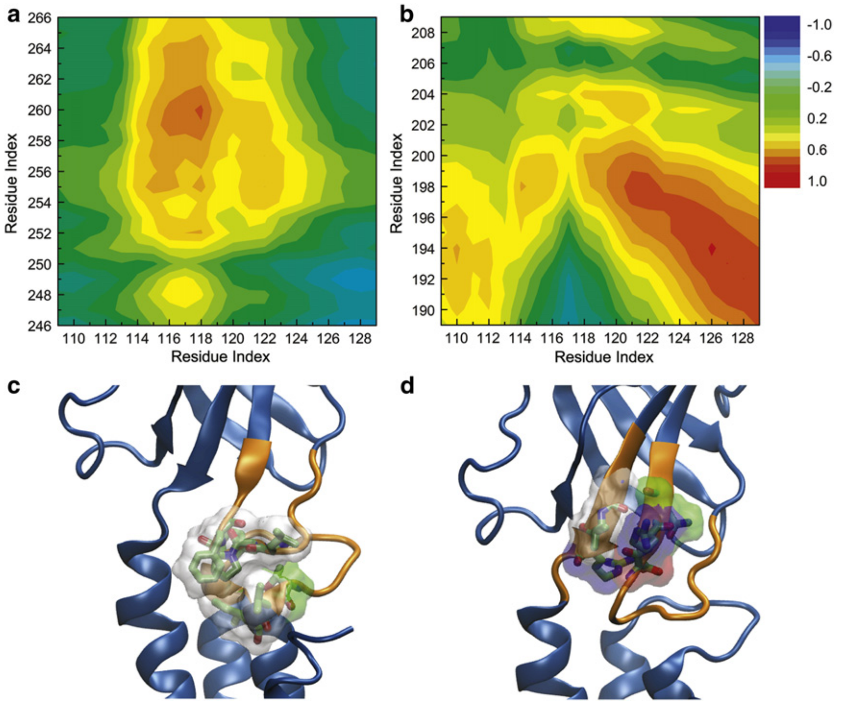

FIGURE 4 Correlated fluctuations of the Cα atoms in ELIC calculated from the MD simulation. The correlation maps are shown for correlated residues from (*a*) the $\beta 6$–$\beta 7$ loop and the M2–M3 linker, with a detailed view of the coupled hydrophobic cluster shown in *c*. (*b*) The $\beta 6$–$\beta 7$ loop and the $\beta 10$–M1 region, with a detailed view of the correlated residues shown in *d*. Residue pairs with a high level of correlated motions are shown in red, orange, and yellow. Anticorrelated motions are represented by the blue/cyan regions. Green color indicates no correlation.

We also observe a strong coupling between the $\beta6$–$\beta7$ loop in one subunit and the $\beta8$–$\beta9$ loop in an adjacent subunit, a coupling feature not seen in the nAChR simulation. This difference reflects the fact that these two loops make closer contacts in the ELIC structure than in the nAChR. A direct electrostatic interaction involving Arg^{117} (in $\beta6$–$\beta7$) and Glu^{156} ($\beta8$–$\beta9$) may provide an effective means of intersubunit communication, whereby the $\beta8$–$\beta9$ loop contributes to channel gating. The lack of such a correlation in the nAChR may indicate mechanistic or functional differences between the two receptors, but may also be due to the deficiency of the nAChR model employed in the simulation (30), in which the $\beta8$–$\beta9$ loop is highly disordered based on the original cryo-EM structure, and part of the loop is built via loop modeling.

A previous correlation analysis on nAChR (30) indicated that both the Cys and $\beta1$–$\beta2$ loops undergo highly concerted movements with the M2–M3 linker, supporting a mechanism whereby the $\beta1$–$\beta2$ and Cys loops might together coordinate communication between the ligand-binding and transmembrane domains. Our simulation of ELIC shows a much weaker correlation between the $\beta1$–$\beta2$ loop and the other two corresponding regions. Indeed, the $\beta1$–$\beta2$ loop in ELIC is farther from the Cys and $\alpha2$–$\alpha3$ loops. ELIC also lacks a global bending motion hinged at the membrane interface that can potentially bring $\beta1$–$\beta2$ closer to $\alpha2$–$\alpha3$, as observed in the nAChR simulation. These two factors contribute to a weaker coupling between $\beta1$–$\beta2$ and the other two loops in ELIC.

Dynamics of the transmembrane helices

The transmembrane helices in the nAChRs are expected to undergo structural rearrangements during gating. However, the precise details and extent of these rearrangements, as well as how they are initiated as a consequence of ligand binding, are still poorly understood. Various structural rearrangements, including rotation, tilting, and kinking of the pore-lining helices, have been proposed. Structural changes inferred from cryo-EM images of the *Torpedo* receptor with and without ACh bound suggested a rotation of the five M2 helices, causing collapse of a central hydrophobic girdle (14,15). However, subsequent studies yielded a mixed picture. Patterns of Zn^{2+} ion binding within the pore suggested a rigid tilting of the M2 helices (53), and a simple dilation mechanism was supported by studies in which *pKa* shifts of transmembrane residues were determined after lysine/histidine substitution (54,55). Controversy also exists as to the location of the gate. The cryo-EM *Torpedo* nAChR structure shows a constriction in the middle of the pore but not complete occlusion. The so-called ‘‘hydrophobic gate’’ idea was supported by subsequent simulations showing that even though the pore is not completely occluded, translocation of cations is essentially blocked (56,57). On the other hand, Zn^{2+} ion probe experiments indicate that the gate is close to the $-1'$ position, near the intracellular end of the pore (53). The existence of two separate gates in the channel—one for the ‘‘resting’’ state and one for the ‘‘desensitized’’ state—has also been proposed based on substituted cysteine accessibility analysis experiments (3).

Using the same rigid-body fitting procedure as described previously (30), we monitored the rotation, kink, and tilting motions of the five $\alpha2$ helices during the simulation. Overall, the pore-lining helices undergo less motion than those of the nAChR (30), even when compared with the recent simulation results of the nAChR with all of the transmembrane binding sites occupied by cholesterol molecules (Fig. S3) (46). Similar to what was observed in the nAChR, no kinking or rotation about the channel axis is evident from the simulation. The time evolution of the tilting motion of $\alpha2$ is depicted in Fig. 5. It indicates an average tilt angle of 11° with respect to the bilayer normal, which is very comparable to that of the nAChR. Between the two tilting components, the radial tilting is almost not present (~1°; Fig. 5 *c*), whereas the average lateral tilting shows a more pronounced magnitude of ~11° (Fig. 5 *a*). The fluctuations of both lateral and radial tilting are much smaller compared with those of the nAChR (MSD 1.5° vs. 5.1° for the lateral tilt, and 1.2° vs. 5.7° for the radial tilt).

Color-coded changes in pore radius along the channel axis are depicted in Fig. 6 *a* as a function of time. Two horizontal stripes enriched in cyan and blue (*z*-axis positions 19 Å and 31 Å) indicate the narrowest regions, which correspond to rings of the hydrophobic residues F246 (20′) and F235 (9′), respectively. Overall, the pore radius is more constrictive than in the nAChR. The minimum pore size remains ~1.4 Å throughout the simulation, which is ~1 Å narrower than that observed in the nAChR. In similarity to the nAChR,

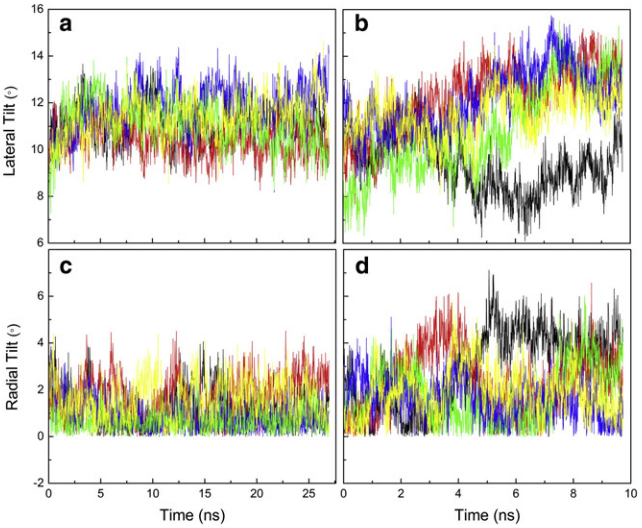

FIGURE 5 Tilting motions of the five M2 helices as a function of time during the MD simulations: (*a*) lateral tilt for ELIC, (*b*) lateral tilt for the F246E mutant, (*c*) radial tilt for ELIC, and (*d*) radial tilt for the F246E mutant.

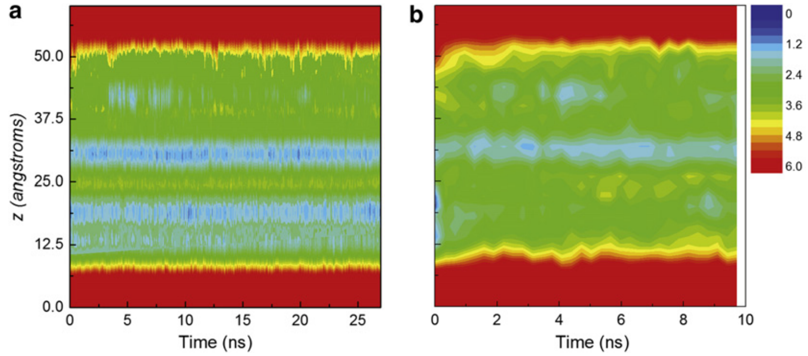

FIGURE 6 Time trajectories of pore size from the MD simulations of (*a*) ELIC and (*b*) the F246E mutant. The vertical axis indicates the *z*-axis position of the channel. The size of the pore is color-coded, with red corresponding to large values and blue corresponding to small values.

the location of the minimum pore radius also alternates between the 20′ position near the extracellular vestibule of the pore and position 9′ in the middle of the pore, whereas the intracellular end of the pore remains wide open (>3.5 Å) all of the time.

A previous simulation of the α7 nAChR revealed penetration of water molecules throughout the pore (30). In sharp contrast, our simulation of ELIC indicated that part of the channel pore (from position 20′ to 9′) was never occupied by any water molecules during the entire length of the simulation. The density profiles are illustrated in Fig. 7 *a* for different types of atoms along the bilayer normal. The extent of the bilayer is clearly delineated by the peaks of the lipid headgroup nitrogen and phosphorus atoms. It is evident that ELIC has a much lower water density compared with the nAChR, with water density close to zero in the middle of the channel. In the nAChR simulation, although L9′ and V13′ initially present an energetic barrier for water penetration, the hydrophobic girdle can easily be disrupted by side-chain movements, which seem to be facilitated by the global bending motion and the associated downward shift of M2. By contrast, the ELIC channel is substantially more hydrophobic and constricted at the extracellular end of the channel. In particular, a ring of five F20′ forms a well-packed hydrophobic cluster that blocks entry of water. Further, the less-hydrated ELIC channel can also be partially attributed to the less-dynamic α2 helices, indicating a direct interplay between pore hydration and dynamics. In fact, no large-scale helix motion is observed during the ELIC simulation, and even the side chains of the pore-lining residues L13′ and F9′ do not move (sideways) as much as in the nAChR simulation. Consistent with previous results from the nAChR, the intracellular end of the pore remains wide open and is especially well hydrated. Our simulation results for ELIC therefore support the proposition that a hydrophobic gate should be present between positions 20′ and 9′, and disfavor the existence of an intracellular gate.

F246E mutant structure

One sharp difference in the alignment of the M2 and α2 sequences is that residue Glu at the 20′ position of the nAChR is replaced by residue Phe in ELIC. To assess the effect of a mutation from charged to hydrophobic on the dynamics and hydration of the pore, we carried out an additional simulation of the F246E mutant. As shown in Fig. 1 *a*, the introduction of E20′ in ELIC increases the dynamics of the α2 transmembrane helices. The fluctuations of both the lateral and radial tilts of the α2 helix become more significant (Fig. 5, *b* and *d*). Notably, the fluctuations of the lateral tilt increases by 2.2° relative to the wild-type ELIC, drawing closer to the value of 5.1° obtained from the nAChR simulation. We also found more pronounced motions of the side chains of F9′ and L13′ in the middle of pore. In the E20′ mutant, these hydrophobic side chains occasionally face away from the channel lumen and pack against another hydrophobic side chains from the neighboring α1 helices.

The pore-size profile of the ELIC mutant (Fig. 6 *b*) shows a much wider pore throughout the length of the transmembrane domain. The blue strip at the 19 Å position, corresponding to the E20′ mutation, has completely disappeared. The narrowest part of the pore is now restricted to the 31 Å position in the plot, corresponding to F9′. Compared with ELIC, however, even the pore size at this position has substantially increased, due to the displacement of the α2 helices and especially the movements of the side chains of F9′. Not surprisingly, the water density within the pore increases considerably as well, due to the increase of the pore size. From Fig. 7 *c* (*red line*), it is evident that the pore is hydrated along the entire length, with the position of minimal water density at the center of the pore, corresponding to the hydrophobic girdle formed by F9′, similarly to what is observed in the nAChR. But compared with the nAChR, the mutant ELIC channel is still less hydrated. Indeed, the averaged water density in the central pore region is only ~0.2 of the bulk water density compared to ~0.4 in the nAChR. Visual inspection of the trajectories shows that although the movements of the hydrophobic side chains of F9′ and L13′ created space for water penetration, only three or four individual water molecules occasionally occupy the constriction zone.

The F-to-E mutation at position 20′ clearly increases hydration of the pore. One obvious reason is that the charged side chains of E make more favorable interactions with water

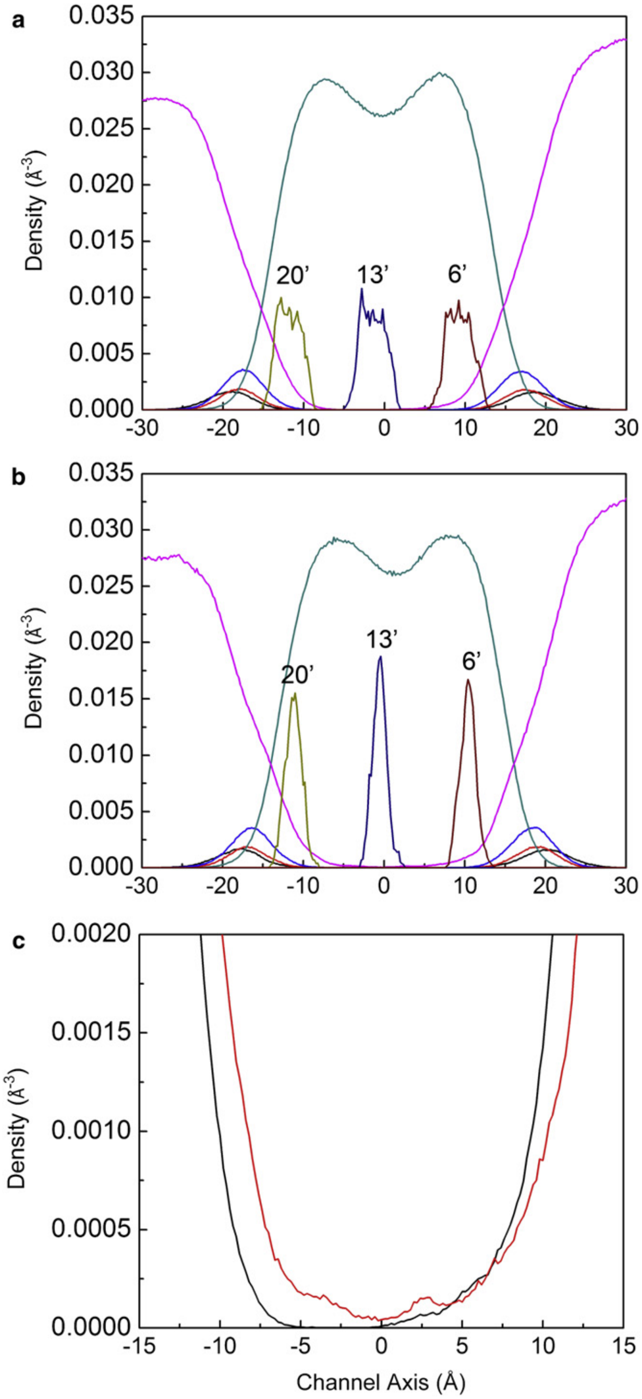

FIGURE 7 Density profiles along the lipid bilayer normal for lipid tail carbon (*green*), lipid headgroup nitrogen (*dark blue*), phosphorus (*red*), and ester oxygen atoms (*blue*), as well as water oxygen atoms (*pink*) for (*a*) ELIC and (*b*) the F246F mutant. (*c*) Amplified version of the density profiles for water oxygen atoms in ELIC (*black*) and the F246E mutant (*red*). Average positions of M2 pore-lining residues F20′, L13′, and Q6′ are shown with yellow, purple, and brown lines, respectively.

molecules than F, thus attracting water molecules. Additionally, the negative charges carried by all five E residues tend to repel each other, thus creating room at the extracellular entrance for water to come through. Finally, another important factor contributing to the increased hydration is the enhanced dynamics of the mutant transmembrane domain, consistent with our previous findings that the dynamics of the pore is a necessary condition for ion conduction (31). The hydrophobic packing of five F residues is energetically favorable and therefore helps stabilize the channel and block water passage. When all five residues are mutated to E, the channel becomes much more dynamic, exhibiting more significant tilting of the pore-lining helices, as well as side-chain movements. We estimate that the hydrophobic stabilization of the five F residues arises from the increase in buried surface area. Each square angstrom of buried hydrophobic surface within a folded protein is expected to contribute ~24 cal/mol toward the free energy of protein folding (58). In ELIC, the total buried surface area for five F side chains is ~670 Å^2, which yields a total packing energy of ~16 kcal/mol. Even though the calculation is approximate, it supports the idea that hydrophobic interactions contribute significantly to the overall stability of the five-α2 helix bundle. The increased stability of five helices in closer contact in turn creates a greater barrier for water and ions to overcome. Although charged residues (e.g., E) at 20′ position has not been identified as a determinant of charge selectivity in the nAChR, it would help concentrate oppositely-charged ions in the extracellular vestibule, thereby affecting channel conductance after mutation of these residues (59,60).

Altogether, our simulation of the F246E mutant (a primitive nAChR model) suggests that the ELIC channel has a reduced single-channel conductance and would require more significant structural rearrangements of the α2 helices to conduct ions, consistent with the observations that the ELIC channel shows slower kinetics of activation as well as lower gating efficiency (21,22).

CONCLUSIONS

In this study, we probed the structural dynamics and hydration of the bacterial pentameric LGIC ELIC. Previous experimental data established that ELIC shares considerable sequence homology to the nAChR and possesses a minimal ‘‘core’’ structure needed to function as an LGIC. The recently determined crystal structure of ELIC further demonstrates that the ELIC structure remarkably resembles that of the nAChR. From a dynamical perspective, our simulation confirms that ELIC exhibits substantial similarity to the nAChR in both its structural flexibility profile and overall residue-residue dynamical coupling features, which supports the idea that ELIC possesses a robust architecture needed for gating function.

On the other hand, ELIC showed much reduced motion in the simulation, especially in its transmembrane domain. Although some of the enhanced dynamics observed in the nAChR may arise from the method used to solve the structure and/or the absence of cholesterol in the transmembrane-binding sites during simulation, a comparison of the simulation results reveals that not all of the enhanced dynamics can be attributed to the deficiency of the nAChR model. A significant portion of the dynamical differences between the nAChR and ELIC clearly stem from structural differences, such as the extracellular regions that are distant from the cholesterol-binding sites, which are not significantly affected by the presence of cholesterol. Although comparable mobility in these regions is observed in the simulations of the nAChR with and without binding of cholesterol at the A, B, C sites, both simulations show greater fluctuations than ELIC (Fig. S3). Even for some of transmembrane regions, especially in the $\alpha 2$/M2 helices, ELIC still fluctuates less than the nAChR simulated in the presence of cholesterol (see the navy box highlighted in Fig. S3, c and d) (46). Several structural factors may contribute to the increased stability of ELIC. First, the subunit interfaces in ELIC are more compact than in the nAChR. Indeed, the cryo-EM model of the *Torpedo* nAChR is more loosely packed with a less tightly closed pore. Its adjacent pore-lining helices also appear to assume an unfavorable parallel helix-helix packing. A second stabilizing factor may be the existence of a hydrophobic core in the ligand-binding domain. The residue pair Val^{35} and Phe^{110}, buried inside the β-sandwich core of ELIC, considerably increases the local stability and may therefore contribute to the overall stability of protein. Finally, a ring of well-packed Phe residues, located at the extracellular entrance of the pore, appears to greatly reduce tilting motions of the transmembrane helices, thus increasing the overall stability. The simulation of an F246E mutant confirms that the five F residues at position $20'$ not only increase the stability of ELIC, but also reduce hydration of the pore. Available structural information regarding the nAChR suggests that the gating movements are quite small, with part of the receptor predisposed in a destabilized state. Hence, the increased stability in ELIC may account for its slow activation and low conductance.

Although a similar global twisting motion is observed in ELIC, displacements of atom coordinates along the major mode do not appear to widen the pore constriction as much as they do in nAChR. Two clusters of bulky hydrophobic residues at positions $20'$ and $9'$ are more proximal in the crystal structure and remain less dynamic during the simulation. From these observations, it follows that the ELIC transmembrane helices would involve more significant structural arrangements to open this bacterial channel. A pure tilting motion or simple dilation (or a small structural rearrangement) would appear unlikely to do so. Our simulation of ELIC also shows altered dynamical behavior and coupling features for some residues at membrane interface regions that might mediate transduction between binding and pore domains. Given these dynamical differences, along with notable differences in residue composition in these key regions contributing to gating, it remains puzzling whether the two types of receptors employ the same mechanism for propagating structural changes through the membrane interface regions. The basic allosteric motion seems well conserved. However, the bacterial receptor, an ancestral member within the superfamily, likely employs a modified transduction mechanism, given its slow rate of activation and lack of desensitization.

Finally, water density profiles show that the ELIC pore is only partially water-filled, with the extracellular vestibule of the channel depleted of water molecules, in sharp contrast to the nAChR, where the channel is fully hydrated. Indeed, the extracellular entrance of the ELIC channel is occupied by rings of bulky hydrophobic side chains that occlude a nonhydrated cavity extending from the extracellular border to the center of the pore, whereas the corresponding region in the nAChR is wider and appears to accommodate multiple sodium ions through interactions with two rings of negatively charged residues. Although it has been speculated that the nAChR may not be imaged in a completely ‘‘closed’’ state, there is little doubt that the ELIC structure is in a nonconducting state.

SUPPORTING MATERIAL

Three figures and one image are available at http://www.biophysj.org/biophysj/supplemental/S0006-3495(09)00754-1.

We are indebted to Grace Brannigan and Jerome Henin for kindly providing us with detailed data from their previous study (46).

X.C. is funded by the Computer Science and Mathematics Division at Oak Ridge National Laboratory. This work was supported by grants from the National Institutes of Health (GM31749, NSF MCB-0506593, and MCA93S013 to J.A.M.). Additional support to J.A.M. for this project was provided partly by the Howard Hughes Medical Institute, the San Diego Supercomputer Center, the National Biomedical Computation Resource, and the National Science Foundation Center for Theoretical Biological Physics.

REFERENCES

1. Sine, S., and A. Engel. 2006. Recent advances in Cys-loop receptor structure and function. *Nature*. 440:448–455.
2. Corringer, P., N. Le Novere, and J. Changeux. 2000. Nicotinic receptors at the amino acid level. *Annu. Rev. Pharmacol. Toxicol.* 40:431–458.
3. Karlin, A. 2002. Emerging structure of the nicotinic acetylcholine receptors. *Nat. Rev. Neurosci.* 3:102–114.
4. Blokland, A. 1995. Acetylcholine: a neurotransmitter for learning and memory? *Brain Res. Brain Res. Rev.* 21:285–300.
5. Clementi, F., D. Fornasari, and C. Gotti. 2000. Neuronal nicotinic receptors, important new players in brain function. *Eur. J. Pharmacol.* 393:3–10.
6. Hogg, R., M. Raggenbass, and D. Bertrand. 2003. Nicotinic acetylcholine receptors: from structure to brain function. *Rev. Physiol. Biochem. Pharmacol.* 147:1–46.
7. Grutter, T., N. Le Novere, and J. Changeux. 2004. Rational understanding of nicotinic receptors drug binding. *Curr. Top. Med. Chem.* 4:645–650.
8. Cassels, B., I. Bermudez, F. Dajas, J. Abin-Carriquiry, and S. Wonnacott. 2005. From ligand design to therapeutic efficacy: the challenge for nicotinic receptor research. *Drug Discov. Today.* 10:1657–1665.
9. Karlin, A., and M. Akabas. 1995. Toward a structural basis for the function of nicotinic acetylcholine receptors and their cousins. *Neuron.* 15:1231–1244.

10. Sine, S. 2002. The nicotinic receptor ligand binding domain. *J. Neurobiol.* 53:431–446.
11. Corringer, P., S. Bertrand, J. Galzi, A. Devillers-Thiery, J. Changeux, et al. 1999. Mutational analysis of the charge selectivity filter of the α7 nicotinic acetylcholine receptor. *Neuron.* 22:831–843.
12. Auerbach, A., and G. Akk. 1998. Desensitization of mouse nicotinic acetylcholine receptor channels. A two-gate mechanism. *J. Gen. Physiol.* 112:181–197.
13. Grosman, C., and A. Auerbach. 2001. The dissociation of acetylcholine from open nicotinic receptor channels. *Proc. Natl. Acad. Sci. USA.* 98:14102–14107.
14. Unwin, N. 2005. Refined structure of the nicotinic acetylcholine receptor at 4A resolution. *J. Mol. Biol.* 346:967–989.
15. Miyazawa, A., Y. Fujiyoshi, and N. Unwin. 2003. Structure and gating mechanism of the acetylcholine receptor pore. *Nature.* 423:949–955.
16. Brejc, K., W. van Dijk, R. Klaassen, M. Schuurmans, J. van Der Oost, et al. 2001. Crystal structure of an ACh-binding protein reveals the ligand-binding domain of nicotinic receptors. *Nature.* 411:269–276.
17. Celie, P., S. van Rossum-Fikkert, W. van Dijk, K. Brejc, A. Smit, et al. 2004. Nicotine and carbamylcholine binding to nicotinic acetylcholine receptors as studied in AChBP crystal structures. *Neuron.* 41:907–914.
18. Hansen, S., G. Sulzenbacher, T. Huxford, P. Marchot, P. Taylor, et al. 2005. Structures of Aplysia AChBP complexes with nicotinic agonists and antagonists reveal distinctive binding interfaces and conformations. *EMBO J.* 24:3635–3646.
19. Bourne, Y., T. Talley, S. Hansen, P. Taylor, and P. Marchot. 2005. Crystal structure of a Cbtx-AChBP complex reveals essential interactions between snake α-neurotoxins and nicotinic receptors. *EMBO J.* 24:1512–1522.
20. Dellisanti, C., Y. Yao, J. Stroud, Z. Wang, and L. Chen. 2007. Crystal structure of the extracellular domain of nAChR α1 bound to α-bungarotoxin at 1.94 A resolution. *Nat. Neurosci.* 10:953–962.
21. Hilf, R., and R. Dutzler. 2008. X-ray structure of a prokaryotic pentameric ligand-gated ion channel. *Nature.* 452:375–379.
22. Bocquet, N., L. de Carvalho, J. Cartaud, J. Neyton, C. Le Poupon, et al. 2007. A prokaryotic proton-gated ion channel from the nicotinic acetylcholine receptor family. *Nature.* 445:116–119.
23. Henchman, R., H. Wang, S. Sine, P. Taylor, and J. McCammon. 2005. Ligand-induced conformational change in the {α}7 nicotinic receptor ligand binding domain. *Biophys. J.* 88:2564–2576.
24. Henchman, R., H. Wang, S. Sine, P. Taylor, and J. McCammon. 2003. Asymmetric structural motions of the homomeric α7 nicotinic receptor ligand binding domain revealed by molecular dynamics simulation. *Biophys. J.* 85:3007–3018.
25. Hung, A., K. Tai, and M. Sansom. 2005. Molecular dynamics simulation of the M2 helices within the nicotinic acetylcholine receptor transmembrane domain: structure and collective motions. *Biophys. J.* 88:3321–3333.
26. Saladino, A., Y. Xu, and P. Tang. 2005. Homology modeling and molecular dynamics simulations of transmembrane domain structure of human neuronal nicotinic acetylcholine receptor. *Biophys. J.* 88:1009–1017.
27. Xu, Y., F. Barrantes, X. Luo, K. Chen, J. Shen, et al. 2005. Conformational dynamics of the nicotinic acetylcholine receptor channel: a 35-ns molecular dynamics simulation study. *J. Am. Chem. Soc.* 127:1291–1299.
28. Yi, M., H. Tjong, and H. Zhou. 2008. Spontaneous conformational change and toxin binding in α7 nicotinic acetylcholine receptor: insight into channel activation and inhibition. *Proc. Natl. Acad. Sci. USA.* 105:8280–8285.
29. Law, R., R. Henchman, and J. McCammon. 2005. A gating mechanism proposed from a 15 nanosecond simulation of a complete human α7 nicotinic acetylcholine receptor model. *Proc. Natl. Acad. Sci. USA.* 102:6813–6818.
30. Cheng, X., I. Ivanov, H. Wang, S. Sine, and J. McCammon. 2007. Nanosecond-timescale conformational dynamics of the human α7 nicotinic acetylcholine receptor. *Biophys. J.* 93:2622–2634.
31. Wang, H., X. Cheng, P. Taylor, J. McCammon, and S. Sine. 2008. Control of cation permeation through the nicotinic receptor channel. *PLoS Comput. Biol.* 4:e41.
32. Cheng, X., B. Lu, B. Grant, R. Law, and J. McCammon. 2006. Channel opening motion of α7 nicotinic acetylcholine receptor as suggested by normal mode analysis. *J. Mol. Biol.* 355:310–324.
33. Cornell, W., P. Cieplak, C. Bayly, I. Gould, K. Merz, et al. 1995. A second generation force field for the simulation of proteins, nucleic acids, and organic molecules. *J. Am. Chem. Soc.* 117:5179–5197.
34. Case, D., T. Darden, T. Cheatham III, C. Simmerling, J. Wang, et al. 2004. AMBER8. University of California, San Francisco.
35. http://agknapp.chemie.fu-berlin.de/karlsberg/.
36. Phillips, J., R. Braun, W. Wang, J. Gumbart, E. Tajkhorshid, et al. 2005. Scalable molecular dynamics with NAMD. *J. Comput. Chem.* 26:1781–1802.
37. MacKerrell, A., D. Bashford, M. Bellott, R. Dunbrack, J. Evanseck, et al. 1998. All-atom empirical potential for molecular modeling and dynamics studies of proteins. *J. Phys. Chem. B.* 102:3586–3616.
38. Darden, T., D. York, and L. Pedersen. 1993. Particle mesh Ewald: an N log (N) method for Ewald sums in large systems. *J. Chem. Phys.* 98:10089–10092.
39. Tuckerman, M., B. Berne, and G. Martyna. 1992. Reversible multiple time scale molecular dynamics. *J. Chem. Phys.* 97:1990–2001.
40. Ryckaert, J., G. Ciccotti, and H. Berendsen. 1977. Numerical integration of the Cartesian equations of motion of a system with constraints: molecular dynamics of n-alkanes. *J. Comput. Phys.* 23:327–341.
41. Van Der Spoel, D., E. Lindahl, G. Groenhof, A. Mark, and H. Berendsen. 2005. GROMACS: fast, flexible, and free. *J. Comput. Chem.* 26:1701–1718.
42. Origin 7.5, www.originlab.com: Northampton, MA.
43. Lipari, G., and A. Szabo. 1982. Model-free approach to the interpretation of nuclear magnetic resonance relaxation in macromolecules. 1. Theory and range of validity. *J. Am. Chem. Soc.* 104:4546–4559.
44. Smart, O., J. Neduvelil, X. Wang, B. Wallace, and M. Sansom. 1996. HOLE: a program for the analysis of the pore dimensions of ion channel structural models. *J. Mol. Graph.* 14:354–360.
45. Humphrey, W., A. Dalke, and K. Schulten. 1996. VMD: visual molecular dynamics. *J. Mol. Graph. Model.* 14:33–38.
46. Brannigan, G., J. Henin, R. Law, R. Eckenhoff, and M. Klein. 2008. Embedded cholesterol in the nicotinic acetylcholine receptor. *Proc Natl Acad Sci USA.* 105:14418–14423.
47. Gao, F., N. Bren, T. Burghardt, S. Hansen, R. Henchman, et al. 2005. Agonist-mediated conformational changes in acetylcholine-binding protein revealed by simulation and intrinsic tryptophan fluorescence. *J. Biol. Chem.* 280:8443–8451.
48. Mitra, A., T. Bailey, and A. Auerbach. 2004. Structural dynamics of the M4 transmembrane segment during acetylcholine receptor gating. *Structure.* 12:1909–1918.
49. Law, R., D. Tieleman, and M. Sansom. 2003. Pores formed by the nicotinic receptor m2δ peptide: a molecular dynamics simulation study. *Biophys. J.* 84:14–27.
50. Henzler-Wildman, K., M. Lei, V. Thai, S. Kerns, M. Karplus, et al. 2007. A hierarchy of timescales in protein dynamics is linked to enzyme catalysis. *Nature.* 450:913–916.
51. Taly, A., M. Delarue, T. Grutter, M. Nilges, N. Le Novere, et al. 2005. Normal mode analysis suggests a quaternary twist model for the nicotinic receptor gating mechanism. *Biophys. J.* 88:3954–3965.

52. Taly, A., P. Corringer, T. Grutter, L. Prado de Carvalho, M. Karplus, et al. 2006. Implications of the quaternary twist allosteric model for the physiology and pathology of nicotinic acetylcholine receptors. *Proc. Natl. Acad. Sci. USA.* 103:16965–16970.
53. Paas, Y., G. Gibor, R. Grailhe, N. Savatier-Duclert, V. Dufresne, et al. 2005. Pore conformations and gating mechanism of a Cys-loop receptor. *Proc. Natl. Acad. Sci. USA.* 102:15877–15882.
54. Cymes, G., Y. Ni, and C. Grosman. 2005. Probing ion-channel pores one proton at a time. *Nature.* 438:975–980.
55. Cymes, G., and C. Grosman. 2008. Pore-opening mechanism of the nicotinic acetylcholine receptor evinced by proton transfer. *Nat. Struct. Mol. Biol.* 15:389–396.
56. Ivanov, I., X. Cheng, S. Sine, and J. McCammon. 2007. Barriers to ion translocation in cationic and anionic receptors from the Cys-loop family. *J. Am. Chem. Soc.* n press.
57. Beckstein, O., and M. Sansom. 2006. A hydrophobic gate in an ion channel: the closed state of the nicotinic acetylcholine receptor. *Phys. Biol.* 3:147–159.
58. Chothia, C. 1975. Structural invariants in protein folding. *Nature.* 254:304–308.
59. Imoto, K., C. Busch, B. Sakmann, M. Mishina, T. Konno, et al. 1988. Rings of negatively charged amino acids determine the acetylcholine receptor channel conductance. *Nature.* 335:645–648.
60. Kienker, P., G. Tomaselli, M. Jurman, and G. Yellen. 1994. Conductance mutations of the nicotinic acetylcholine receptor do not act by a simple electrostatic mechanism. *Biophys. J.* 66:325–334.